

Transferable interatomic potential for aluminum from ambient conditions to warm dense matter

Sandeep Kumar^{1,2,*}, Hossein Tahmasbi^{1,2}, Kushal Ramakrishna^{1,2}, Mani Lokamani,² Svetoslav Nikolov,³ Julien Tranchida,⁴ Mitchell A. Wood,³ and Attila Cangi^{1,2,†}¹Center for Advanced Systems Understanding (CASUS), D-02826 Görlitz, Germany²Helmholtz-Zentrum Dresden-Rossendorf (HZDR), 01328 Dresden, Germany³Computational Multiscale Department, Sandia National Laboratories, Albuquerque 87185, New Mexico, USA⁴CEA, DES, IRESNE, DEC, SESC, LM2C, F-13108 Saint-Paul-Lez-Durance, France

(Received 21 April 2023; accepted 10 August 2023; published 6 September 2023)

We present a study on the transport and material properties of aluminum spanning from ambient to warm dense matter conditions using a machine-learned interatomic potential (ML-IAP). Prior research has utilized ML-IAPs to simulate phenomena in warm dense matter, but these potentials have often been calibrated for a narrow range of temperatures and pressures. In contrast, we train a single ML-IAP over a wide range of temperatures, using density functional theory molecular dynamics (DFT-MD) data. Our approach overcomes the computational limitations of DFT-MD simulations, enabling us to study the transport and material properties of matter at higher temperatures and longer time scales. We demonstrate the ML-IAP transferability across a wide range of temperatures using molecular dynamics by examining the ionic part of thermal conductivity, shear viscosity, self-diffusion coefficient, sound velocity, and structure factor of aluminum up to about 60000 K, where we find good agreement with previous theoretical data.

DOI: [10.1103/PhysRevResearch.5.033162](https://doi.org/10.1103/PhysRevResearch.5.033162)

I. INTRODUCTION

Warm dense matter (WDM) is a state of matter characterized by densities ranging from solid density to a few orders higher than solid density and temperatures ranging from a few eV to a few keV [1]. It is defined by two parameters: The ionic Coulomb coupling parameter Γ , which is the ratio of the average kinetic energy to the average potential energy, and the electron degeneracy parameter Θ , which is the ratio of the average kinetic energy to the average Fermi energy. WDM is defined as the region of parameter space where $\Gamma \approx 1$ and $\Theta \approx 1$ [2–5].

The study of WDM is important for advancing our understanding of phenomena that both occur in nature and are generated in the laboratory. In nature, such conditions can be found in the cores of giant planets and exoplanets [6]. In the laboratory, WDM is generated at various facilities around the world, including pulsed power facilities such as the Z-Machine [7] and bright photon sources such as the European X-Ray Free-Electron Laser Facility (European XFEL) [8], the Linac Coherent Light Source (LCLS) [9–11], and the National Ignition Facility (NIF) [12]. Inertial confinement fusion experiments also involve the creation of WDM when fuel capsules are heated towards ignition [1,13].

Modeling and simulating WDM is challenging due to its unique properties, which fall in a regime that is too dense for standard plasma theories and too hot for condensed matter theories to be applicable. To study the dynamical and thermodynamical properties of WDM, DFT-MD simulations have been widely used [14–20]. However, there are several limitations to the use of DFT-MD for this purpose. First, DFT-MD becomes computationally infeasible at higher temperatures, making it difficult to study the properties of WDM under these conditions. Second, finite-size effects, which are caused by the limited number of atoms that can be simulated on current high-performance computing (HPC) platforms (typically a few hundred atoms), can lead to inaccurate results for many observables. Finally, DFT-MD simulations are typically limited to time scales of around 100 ps, making it difficult to accurately study long-timescale phenomena such as ionic transport.

In the past, embedded atom models (EAMs) [21–23] have been proposed as potentials for large-scale MD simulations of WDM [24,25], but they have been found to be inconsistent with DFT-MD simulations over a wide range of temperatures and pressures. Similarly, Yukawa pair potentials, which model ions that are screened by electrons, have been employed to calculate the ion-ion structure factor [26–28] in WDM. However, their utilization of ad hoc corrections does impose limitations on their predictive capabilities.

Recently, MD simulations using machine-learning-based interatomic potentials (ML-IAPs) have been shown to overcome these computational limitations while maintaining the accuracy of DFT-MD simulations [29–35]. These ML-IAPs have the potential to enable the study of thermodynamic properties in WDM at higher temperatures and longer time scales [36–41], enabling a deeper understanding of this important

*s.kumar@hzdr.de

†a.cangi@hzdr.de

state of matter. The material properties the ML-IAP enables us to simulate via large-scale MD simulations are important for understanding the dynamics of planetary interiors and inertial confinement fusion plasmas. For example, the diffusion of particles plays a significant role in fuel degradation during inertial confinement fusion [42], while the thermal conductivity of materials is an important quantity for understanding the cooling process of a planet's core [43–45].

In this study, we use an ML-IAP to simulate ambient aluminum up to very high temperatures corresponding to the WDM regime. Previous research has used ML-IAPs for WDM simulations, but these potentials have often been calibrated for specific temperature and pressure ranges [37,39,40,46]. In contrast, we train a single ML-IAP that can be used across a range of temperatures using DFT-MD data. To generate the ML-IAP, we use the spectral neighbor analysis potential (SNAP) method [31], which represents the local environment of each atom through bispectrum components of the local atomic density projected onto a basis of hyperspherical harmonics in four dimensions. These components serve as descriptors in the SNAP method. We use the DAKOTA optimization software [47] to tune the ML-IAP's hyperparameters, such as the cutoff distance for the potential and the weight of specific training data sets. By using this approach, we are able to accurately simulate ambient aluminum up to very high temperatures corresponding to the WDM regime. We focus our study on aluminum, which has been subject to various experimental measurements [3,48–53].

We center our investigation on assessing the ML-IAP's ability to extrapolate to higher temperatures beyond the range of the training data. In order to evaluate the accuracy of our ML-IAP, we conduct large-scale MD simulations to calculate various properties over a range of temperatures from 300 K (0.0259 eV) to 58022 K (5 eV), including the ionic part of thermal conductivity, shear viscosity, self-diffusion coefficient, sound velocity, and structure factor. In the diffusion coefficient calculation, we extend the mentioned temperature range further up to 116 040 K (10 eV).

Our paper is organized as follows. In Sec. II, we describe the methods used to train the ML-IAP and to calculate the quantities using MD simulations. In Sec. III, we present the results of our investigation on the temperature transferability of the ML-IAP by calculating various transport and material properties. Finally, in Sec. IV, we provide our conclusion.

II. METHODS

A. Generation of the ML-IAP

We generate an ML-IAP based on the SNAP methodology [31,54] for aluminum in a large temperature range. Training data is generated using DFT-MD calculations at ambient mass density (2.7 g/cm³) using simulation cells containing 108 and 256 atoms over a temperature range of 300–10000 K. These simulations are performed using the VASP software package [55–57] with Kohn-Sham orbitals expanded in plane waves and PAW pseudopotentials used for the electron-ion interaction [58–60] with a core radius of $r_c = 1.9 a_B$ where a_B is the

Bohr radius. The plane wave cutoff is set to 450 eV and the convergence in the total energy in each self-consistency cycle is set to 10^{-5} . The PBE exchange-correlation functional [61] is applied throughout. The DFT-MD simulations are run for 10000 steps with a time step of 0.2 fs and are thermostated using the Nosé-Hoover method [62,63]. We investigated the time evolution of the energy and characteristics of the radial distribution function to test the equilibration of the system and found that the system equilibrates around 10000 time steps. We sample the Brillouin zone on a $2 \times 2 \times 2$ grid of k points and Gamma point for the solid and liquid configurations, respectively, and increase the number of bands in the simulations as the temperature increases. The number of bands is varied from 324 at the minimum temperature (300 K) for a supercell containing 108 atoms to 896 at the maximum temperature (10000 K) considered in the data set for a supercell containing 256 atoms. By doing so, we achieve convergence in the total energy in each self-consistency cycle up to 10^{-5} .

In the next step, we create an ML-IAP based on this training data. Following the SNAP methodology, the total energy of the system of N atoms with positions \mathbf{r}^N is decomposed into

$$E(\mathbf{r}^N) = E_{\text{ref}}(\mathbf{r}^N) + \sum_{i=1}^N E_{\text{SNAP}}^i, \quad (1)$$

where E_{ref} denotes a reference potential energy and E_{SNAP}^i the total energy of atom i relative to the atoms in its neighborhood. Here, the presence of the reference potential can improve the accuracy of the potential energy, which need not be parametrized by the training data but can be included from known limiting cases. In this regard, we use the Ziegler-Biersack-Littmark (ZBL) potential [64] as a reference potential. The ZBL model for aluminum is derived from ion stopping power data, thus providing an accurate description of short-range (higher-energy) atomic interactions. The SNAP ML-IAP energy of each atom is expressed as

$$E_{\text{SNAP}}^i = \boldsymbol{\beta} \cdot \mathbf{B}^i \quad (2)$$

in terms of a linear combination of bispectrum components \mathbf{B}^i and linear coefficients β_k . Consequently, the forces on an atom j are calculated from the derivatives of the bispectrum components of atom i with respect to changes in the positions \mathbf{r}^j , which reads

$$F_{\text{SNAP}}^j = -\nabla_j \sum_{i=1}^N E_{\text{SNAP}}^i = -\boldsymbol{\beta} \cdot \sum_{i=1}^N \frac{\partial \mathbf{B}^i}{\partial \mathbf{r}^j}. \quad (3)$$

The bispectrum components \mathbf{B}^i represent the atomic density of those atoms in the neighborhood of atom i with a cutoff distance R_{cut} . They are related to four-dimensional (4D) hyperspherical harmonics and do preserve invariance under symmetry operations [54]. The trainable parameters, $\boldsymbol{\beta}$, of the SNAP ML-IAP are determined by weighted linear regression in an iterative process to reproduce the total energy and atomic forces in each atomic configuration of the DFT-MD training data set. The linear regression is carried out using the FitsNAP software package [65,66]. To this end, we preprocess the DFT-MD data by extracting the total energies and the forces on all

the atoms. The training datasets and parameters are listed in Table S1 [67]. The DFT-MD data is grouped into intervals of 100 K in the temperature range from 300–1000 K, and at intervals of 1000 K from 1000–10000 K. For each temperature, we randomly select approximately 100 snapshots of equilibrated atomic configurations. We include low-temperature data from 300–900 K in the training because a diverse dataset improves the quality of the trained ML-IAP [68]. Based on this data, we generate a SNAP ML-IAP over the desired temperature range.

Finally, we need to determine the hyperparameters of the ML-IAP. These include the cutoff radius R_{cut} , which defines the length scale of the atomic environment considered, J_{max} , which determines the number of terms in the expansion of the atomic density in terms of bispectrum components, and the weights of the energy and force training sets. To fix the number of terms in the expansion, we set $J_{\text{max}} = 3$, which defines the number of descriptors, and used the DAKOTA software package [47] to optimize the remaining parameters. We used the single-objective genetic algorithm (SOGA), a global optimization scheme, with energy and force objective functions within the DAKOTA optimization package [69]. The energy and force objective functions are based on the root mean-square error (RMSE) values provided by FitsNAP. To give more flexibility to the genetic algorithm we also allowed DAKOTA to vary the energy and force weights of each DFT training data set. For the SOGA optimization, we adopt a population size of 100 and set the maximum number of iterations to 10000. The cutoff radius was allowed to vary from 4.8–5.8 Å, whereas both the energy weights (EW) and force weights (FW) were optimized within the range from 0.5/(number of snapshots) to 1.5/(number of snapshots). The DAKOTA iterations were run approximately 1300 times to find the optimal parameters, resulting in a cutoff radius of 5.323 Å and the energy and force weights listed in Table S1 [67]. The FitsNAP potential described here along with the DAKOTA/FitsNAP optimization routine is made publicly available [70], enabling an exact reproduction of the optimization workflow. We use the same workflow for the generation of SNAP ML-IAP as Thompson *et al.* [31] have used.

To assess the accuracy of the SNAP ML-IAP, we compare its predictions of energy and force with the reference DFT-MD values. This comparison is displayed in Fig. 1 as a correlation plot, where the ideal result is a straight line (shown in red). The SNAP predictions (represented by blue points) have a certain spread and tilt around this line, which gives a qualitative measure of the error. The mean absolute error (MAE), root mean-square error (RMSE), and standard deviation in energy values for the trained ML-IAP were 6.27 meV/atom, 8.70 meV/atom, and 72.56 meV/atom, respectively. For the forces, these errors were 0.22 eV/Å, 0.32 eV/Å, and 0.73 eV/Å, respectively. The RMSE in energy and force are also calculated for each data set used in the training, see Table S1 [67]. Furthermore, we plot the histograms of the difference between the SNAP prediction and DFT-MD values in the energy and force, which is displayed in Fig. S1 [67]. The distribution of the errors in the histogram is centered around zero. The comparisons and error values indicate that the trained ML-IAP is accurate and suitable for use in large-scale MD simulations.

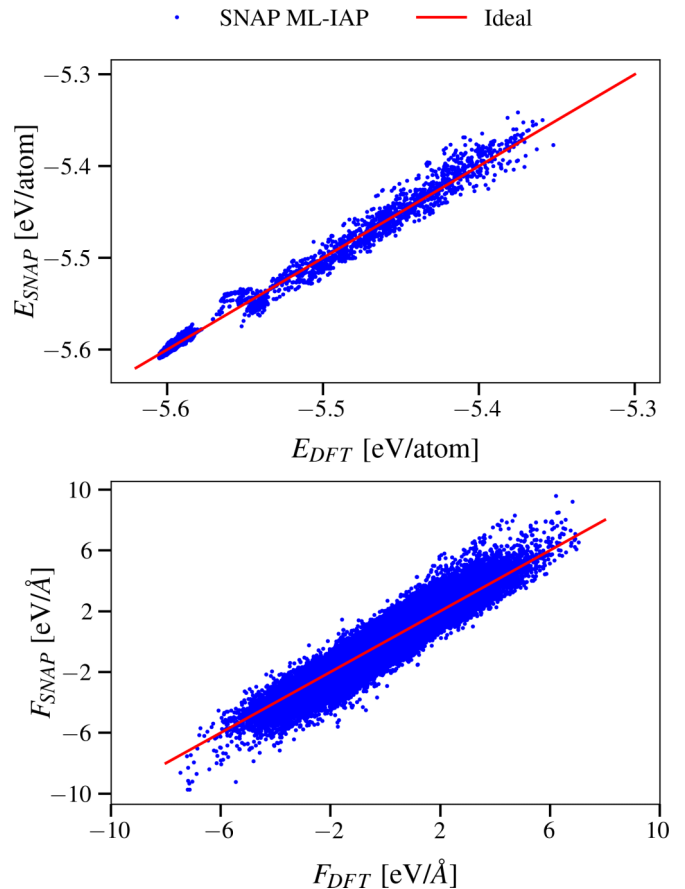


FIG. 1. Correlation plot of the energy (top) and force (bottom) predictions illustrating the qualitative accuracy of the SNAP ML-IAP relative to the DFT-MD reference data.

B. Time-averaged material properties from ML-IAP-driven molecular dynamics simulations

Large-scale MD simulations are carried out using the open-source LAMMPS [71] code. A three-dimensional cubic box with dimensions of $L_x = L_y = L_z = 15a$ (0 to $15a$) along the X , Y , and Z directions is created for the simulations, where a is lattice constant. In the box, we distribute 13500 aluminum atoms in the face-centered cubic (fcc) configuration. The atoms interact with each other via the SNAP ML-IAP and ZBL potential. Periodic boundary conditions are chosen for the simulations. We consider the aluminum atom's mass $m = 26.9815$ u (u is an atomic mass unit), atomic number $Z = 13$, and lattice constant $a = 4.048$ Å. The lattice constant sets the mass density of the aluminum atoms to its ambient value $\rho = 2.7$ g/cm³. We chose the simulation time step as 1 fs, which ensures a fine discretization along the temporal domain and good resolution of the underlying kinetics.

The thermalization of the system is achieved by evolving positions and velocities from a canonical ensemble (NVT) using a Nosé-Hoover [62,63] thermostat. For each temperature, the system is initially evolved in the NVT ensemble for 200 ps to ensure an equilibrium state. After this initial 200 ps NVT run, the atomic configuration achieves thermodynamic equilibrium with the desired temperature and is ready for the transport calculation run. Transport properties are calculated

in the microcanonical ensemble (NVE) on a total time period of 10 ns.

III. RESULTS

The purpose of our study is to evaluate the applicability of the trained SNAP ML-IAP in a wide temperature range, including the challenging conditions of WDM. To achieve this, we analyze various ionic transport and material properties, such as thermal conductivity, shear viscosity, self-diffusion coefficient, sound velocity, and ion-ion structure factor. Our study focuses on aluminum with a fixed mass density of 2.7 g/cm^3 and covers a broad temperature range from 300–58022 K (along an isochore). To assess the accuracy of the SNAP ML-IAP, we test its performance both within and outside the range of the provided training data.

A. Thermal conductivity

We compute the lattice contribution to the thermal conductivity κ from the well-known Green-Kubo formula [72,73]

$$\kappa = \frac{V}{3k_B T^2} \int_0^\infty \langle \mathbf{J}(t) \mathbf{J}(0) \rangle dt. \quad (4)$$

It yields the thermal conductivity from the ensemble average of the autocorrelation $\langle \mathbf{J}(t) \mathbf{J}(0) \rangle$ of the heat flux \mathbf{J} . Here, V denotes the volume, k_B the Boltzmann constant, and T the temperature. The heat flux is defined as

$$\mathbf{J} = \frac{1}{V} \left[\sum_{i=1}^N e_i \mathbf{v}_i + \frac{1}{2} \sum_{i<j}^N [\mathbf{F}_{ij}(\mathbf{v}_i + \mathbf{v}_j)] \mathbf{r}_{ij} \right], \quad (5)$$

where e_i , \mathbf{r}_{ij} , \mathbf{v}_i , and \mathbf{F}_{ij} are the per-atom energy (potential and kinetic), the interatomic distance between atoms, velocity, and forces between atoms, respectively. The integration in Eq. (4) is truncated after a sufficiently large time period, which is determined by the decay of the autocorrelation function. We truncate it at 6 ps for low temperatures (300–950 K), at 1.5 ps at 1000 K, and at 1 ps for higher temperatures (1500–58022 K). Taking a large time interval for integration can introduce additional noise into the thermal conductivity [74]. Although there may be challenges associated with computing thermal conductivity in fluids using the Green-Kubo formula [75], we have chosen to utilize this method as a proxy to assess the transferability of our ML-IAP and due to its recent application in a similar context [39].

Figures 2 and 3 display our findings on the temperature-dependent lattice contribution to thermal conductivity. In pure metals, such as aluminum, the thermal conductivity is primarily determined by free electrons, which serve as heat carriers.

The comparison of our low-temperature predictions with the nonequilibrium MD calculation of Zhou *et al.* [76] and the Boltzmann transport equation calculation of Stojanovic *et al.* [77] are shown in Fig. 2. The excellent agreement illustrates the accuracy of our ML-IAP. The agreement with other predictions at elevated temperatures shows that the ML-IAP accurately reproduces the phonon heat conduction across a large range of solid-phase temperatures.

In the range from 300–10000 K, thermal conductivity decreases with an increase in temperature due to enhancement in phonon-phonon scattering, but as the temperature rises

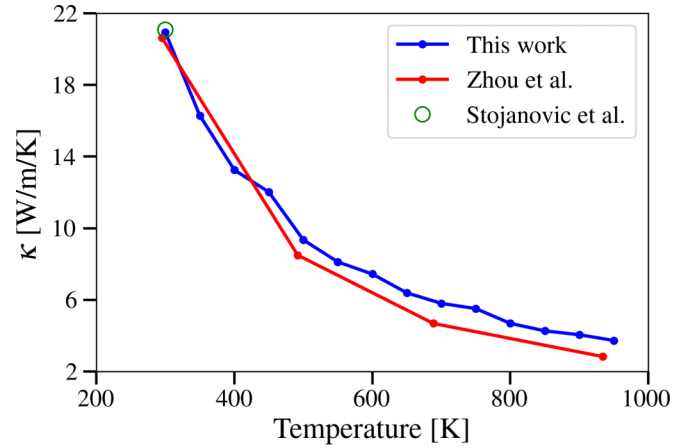


FIG. 2. Lattice thermal conductivity of aluminum at 2.7 g/cm^3 as a function of temperature from 300 K (0.0259 eV) to 950 K (0.0819 eV). We compare our results with the nonequilibrium MD simulation results of Zhou *et al.* [76] and Boltzmann transport equation-based result of Stojanovic *et al.* [77].

(> 10000 K), the thermal motion of atoms dominates resulting in an increase of the thermal conductivity (see Fig. 2 and Fig. 3). In Eq. (4), there is a kinetic and a potential contribution to the thermal conductivity. The kinetic contribution increases with an increase in temperature and dominates in heat transport at higher temperatures (> 10000 K). The vibrational modes scatter in collision with other modes resulting in reduced heat transport. The number of vibrational modes decreases with a decrease in the temperature of the crystal, but due to less scattering, it allows the remaining phonons to travel further, which leads to higher thermal conductivity at a lower temperature.

Next, we compare our predictions with those of Liu *et al.* [37] in Fig. 3. Our analysis indicates that our trained SNAP ML-IAP performs well within the range of the provided

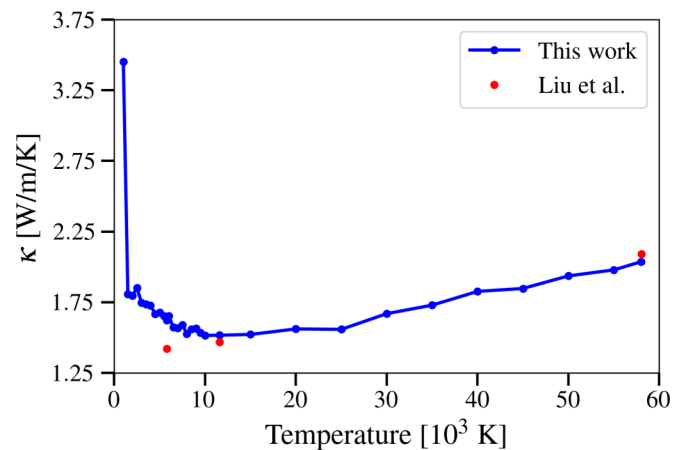


FIG. 3. Lattice thermal conductivity of aluminum at 2.7 g/cm^3 as a function of temperature from 1000 K (0.0862 eV) to 58022 K (5 eV). The SNAP ML-IAP is trained from 300 K (0.0259 eV) to 10000 K (0.861 eV). We compare our results with the results of Liu *et al.* [37], which is calculated by the deep potential molecular dynamics method trained on each temperature.

training data (300–10000 K) and also delivers remarkable accuracy outside this range. However, we observe a significant deviation between our predictions and those of Liu *et al.* at approximately 5802 K (0.5 eV). This difference may be due to noise in the calculation of Liu *et al.* [37] or the use of orbital-free density functional theory (OFDFT) data in their training. OFDFT is appropriate for high temperatures but may become inaccurate at lower temperatures due to the approximations inherent in the kinetic energy functional that dominates the total energy. In the literature, the accuracy of the OFDFT method for WDM has been analyzed by comparing the equation of state data obtained from it to the data obtained from DFT-MD and path-integral Monte Carlo (PIMC) calculations [78–80]. Additionally, it is worth noting that Liu *et al.* [37] trained and assessed their ML-IAP at each temperature displayed in their study, whereas we assess the quality of our ML-IAP outside the range of training data. Despite the sensitivity of thermal conductivity to the interatomic potential, our ML-IAP produces reliable outcomes over a wide temperature range.

Note that a long simulation time is required to calculate a statistically accurate thermal conductivity [81]. Therefore, we ran these calculations for 10 ns before collecting data for processing. A shorter simulation time is possible, but it will require smoothing of data along the temperature axis to suppress noise. We also investigated the effect of finite simulation cell size on thermal conductivity and found that it is negligible for systems with more than 5000 atoms (see Fig. S2 [67]).

B. Viscosity

We also use the Green-Kubo formalism to calculate the shear viscosity

$$\eta = \frac{V}{3k_B T} \int_0^\infty \langle P_{\alpha\beta}(t)P_{\alpha\beta}(0) \rangle dt. \quad (6)$$

Similarly, it is given by an autocorrelation function of the off-diagonal elements of the stress tensor

$$P_{\alpha\beta} = \frac{1}{V} \left[\sum_{i=1}^N \frac{p_i^\alpha p_i^\beta}{m_i} - \sum_i \sum_{i>j} (\alpha_i - \alpha_j) F_{ij} \right], \quad (7)$$

where N is the total number of atoms, p_i^α and p_i^β are the α and β components of the momentum of the i th atom, m_i is the mass of the i th atom, α_i are the Cartesian coordinates of the atoms, F_{ij} are the forces between atoms i and j , and V is the volume of the simulation box. It is important to note that the shear viscosity calculated using the Green-Kubo formula is dependent on the length of the simulation and that longer simulations are required for accurate results.

Figure 4 displays the temperature-dependent shear viscosity of our system. We observe a decreasing trend in viscosity with increasing temperature from 2000–10000 K, followed by a reversal of this trend at temperatures above 10000 K. We compared our results with those obtained with an ML-IAP by Cheng *et al.* [36] and found that our trained ML-IAP accurately predicts the viscosity at the training points, as well as in the intermediate and extrapolation regions.

As with thermal conductivity, the viscosity of our system has both kinetic and potential contributions, as described

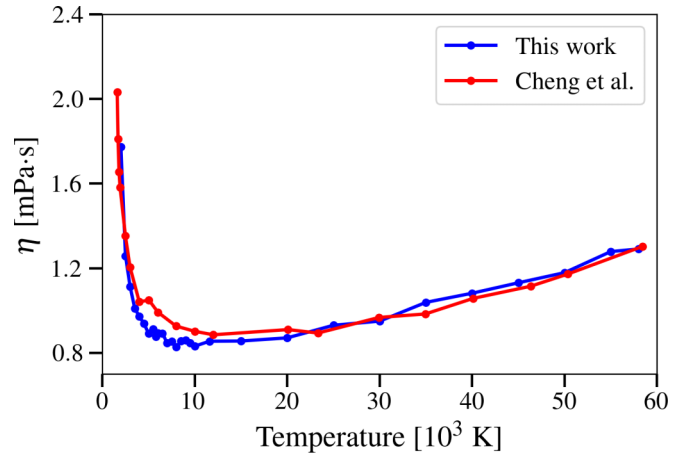


FIG. 4. Shear viscosity of aluminum at 2.7 g/cm^3 as a function of temperature from 2000 K (0.1723 eV) to 58022 K (5 eV). Our values are compared with the shear viscosity values calculated by Cheng *et al.* [36].

by Eq. (7). At lower temperatures, the momentum transport is dominated by the potential contribution, while at higher temperatures, the kinetic contribution becomes more significant. In the intermediate temperature range, both contributions play a role, resulting in longer relaxation times and higher noise levels in the transport properties, even with simulations as long as 10 ns. Nonetheless, our results provide valuable insights into the temperature-dependent behavior of the viscosity of our system.

C. Diffusion coefficient

We also investigate the self-diffusion coefficient, D , which is calculated using the mean-squared displacement of atoms:

$$D = \frac{1}{6t} \left\langle \sum_{i=1}^N [\mathbf{r}_i(t) - \mathbf{r}_i(0)]^2 \right\rangle, \quad (8)$$

where \mathbf{r} is the position of the i th atom at a given time t . The slope of the mean-squared displacement versus time plot gives the values of the diffusion coefficient.

The values of the self-diffusion coefficient as a function of temperature are displayed in Fig. 5. The diffusion coefficient increases with an increase in temperature, which is a direct consequence of the increased thermal motion of aluminum atoms at higher temperatures. We compared our predicted diffusion coefficients with DFT-MD and OFDFT calculations of Sjostrom and Daligault [82] and with kinetic theory calculations of Daligault *et al.* [83]. Our calculations follow the trend in and out of the training data range. Particularly at low temperatures, our predictions agree well with accurate DFT-MD calculations. As temperature increases, our predictions start deviating somewhat from those reported in the literature. The reason for the discrepancy might be due to the use of different levels of theory. As the temperature reaches 116 040 K (10 eV), the difference between our prediction and OFDFT starts decreasing, likely due to the suitability of OFDFT at high temperatures.

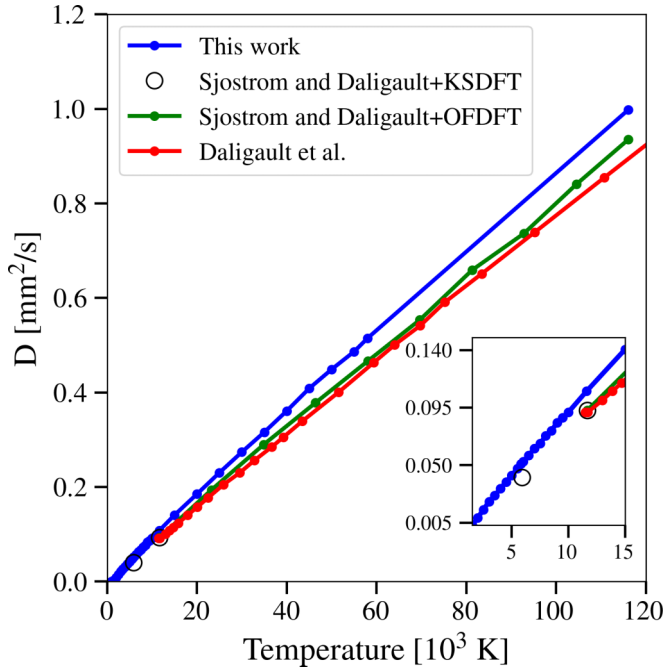


FIG. 5. Self-diffusion coefficient of aluminum at 2.7 g/cm^3 as a function of temperature from 1500 K (0.129 eV) to 116040 K (10 eV). We compare our results with the KSDFT and OFDFT results of Sjostrom and Daligault [82] and kinetic theory-based results of Daligault *et al.* [83]. The values at low temperatures, from 1500 K (0.129 eV) to 10000 K (0.862 eV) are shown in the inset.

Furthermore, we can check the consistency of our result by utilizing the Stokes-Einstein relation [84] as an empirical reference result. It reads $D = k_B T / 2\pi d \eta$ and relates the shear viscosity with the self-diffusion coefficient, where d denotes the diameter of a macroscopic sphere moving with constant velocity in a fluid of a given viscosity. Following Alemany *et al.* [85], we apply this macroscopic concept to our case by determining the value of d from the first peak in the radial distribution function $g(r)$ and using shear viscosity values that were obtained from the Green-Kubo relation. At 10000 K, $d = 2.4975 \text{ \AA}$ and $\eta = 0.8317 \text{ mPa} \cdot \text{s}$, the Stokes-Einstein relation yields a self-diffusion coefficient $0.105 \text{ mm}^2/\text{s}$ which is in good agreement with the calculation of the mean squared displacement yielding a value of $0.091 \text{ mm}^2/\text{s}$.

D. Longitudinal collective modes

1. Sound velocity

The sound velocity of a material at a given temperature can be determined from the slope of the longitudinal dispersion relation $\omega(q)$ in the limit $q \rightarrow 0$ [85,86]. Calculating $\omega(q)$ is computationally expensive because increasingly larger simulation cells are needed as q decreases. Resolving the behavior of $\omega(q)$ at small q becomes feasible in terms of an ML-IAP, which enables us to calculate the dynamics in very large simulation cells and, hence, gather data for small q . The longitudinal current of ions is defined as

$$\lambda(\mathbf{q}, t) = \sum_j v_{jx}(t) e^{i\mathbf{q} \cdot \mathbf{x}_j(t)}, \quad (9)$$

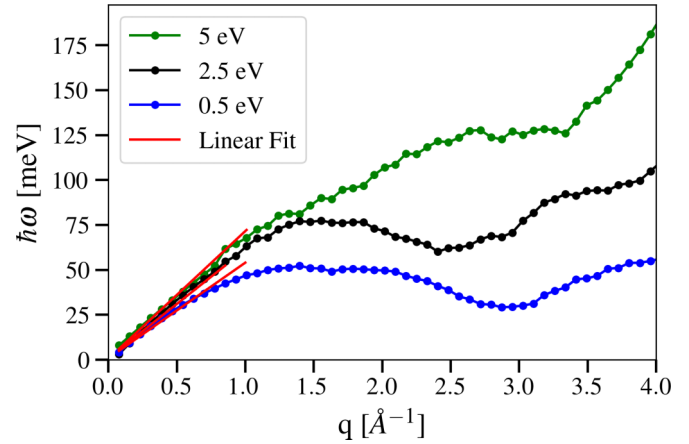


FIG. 6. Dispersion relation of aluminum at mass density of 2.7 g/cm^3 and temperature of 0.5 eV (5802 K), 2.5 eV (29011 K), and 5 eV (58022 K). The slope of the plot (red solid line) in the hydrodynamic regime (small wave vector q) provides sound velocity in the melted aluminum.

where q is the wave vector chosen along the x axis, which depends on integer number n ($n = 1, 2, 3, 4, \dots$) and the simulation system length L_x . The longitudinal current correlation spectrum

$$L(\mathbf{q}, \omega) = \frac{1}{2\pi N} \lim_{\tau \rightarrow \infty} \frac{1}{\tau} |\lambda(\mathbf{q}, \omega)|^2, \quad (10)$$

is then calculated from the longitudinal current spectra, where

$$\lambda(\mathbf{q}, \omega) = \int_0^\tau \lambda(\mathbf{q}, t) e^{-i\omega t} dt \quad (11)$$

denotes the Fourier transform of $\lambda(\mathbf{q}, t)$ and τ the simulation time, which is truncated at a sufficiently large value in our calculations. The peaks in $L(\mathbf{q}, \omega)$ correspond to the collective modes, which represent the maximum energy of the wave mode, see Fig. S3 [67]. The dispersion relation of the longitudinal wave mode can then be obtained by plotting $\omega(q)$ (the value at the peak) versus the wave vector \mathbf{q} , as shown in Fig. 6.

The sound velocity corresponds to the slope at small values for q (linear region). For aluminum at temperatures of 0.5 eV, 2.5 eV, and 5 eV, we determine the sound velocity as 6450 m/s, 8887 m/s, and 9818 m/s, respectively. These values are in agreement with the sound velocities of 6273 m/s and 10365 m/s at 0.5 eV and 5 eV, respectively, obtained previously from OFDFT [27].

2. Ion-ion structure factor

The dynamic ion-ion structure factor (DSF) is obtained from density fluctuations [85,86] and is defined as

$$S(\mathbf{q}, \omega) = \frac{1}{2\pi} \int_{-\infty}^{\infty} F(\mathbf{q}, t) e^{-i\omega t} dt \quad (12)$$

in terms of the intermediate scattering function

$$F(\mathbf{q}, t) = \frac{1}{N} \langle n(\mathbf{q}, t) n(-\mathbf{q}, 0) \rangle \quad (13)$$

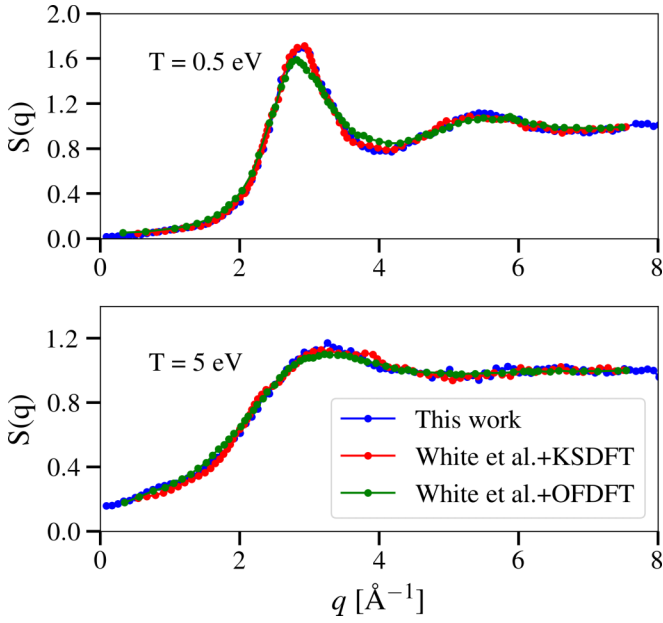


FIG. 7. Static structure factor of aluminum at a mass density of 2.7 g/cm^3 and temperatures of 0.5 eV (5802 K) (top) and 5 eV (58022 K) (bottom). We compare our results (blue curve) with the DFT-MD (red curve) and OFDFT (green curve) results of White *et al.* [27]. Our results are in excellent agreement with the results obtained from DFT-MD.

from atomic density correlations $\langle n(\mathbf{q}, t)n(-\mathbf{q}, 0) \rangle$ obtained from an ensemble average. The atomic density is calculated from the atomic positions as

$$n(\mathbf{q}, t) = \sum_j e^{i\mathbf{q}\cdot\mathbf{x}_j(t)}. \quad (14)$$

Finally, the initial value of the intermediate scattering function yields the static structure factor (SSF)

$$S(\mathbf{q}) = F(\mathbf{q}, t = 0). \quad (15)$$

Both the SSF and the DSF are measured in experiments, for example, using neutron scattering or x-ray diffraction. Both are used for the diagnostics of the temperature, density, and ionization state in dense plasmas and WDM [87]. Rüter and Redmer [88] have calculated the ion-ion structure factor for warm dense aluminum using DFT-MD calculations. In this work, we compute the DSF and the SSF by postprocessing our MD data with the DYNASOR code [89].

First, we illustrate the SSF as a function of wave vector q for temperatures of 0.5 eV (5802 K) and 5 eV (58022 K) in Fig. 7 and compare our results with those from DFT-MD and OFDFT [27]. Note the excellent agreement of our prediction with the DFT-MD result at 0.5 eV (5802 K) and inaccuracies of the OFDFT result in the main peak. This confirms the abilities of our SNAP ML-IAP to interpolate accurately in the range of training data. Furthermore, we observe excellent agreement of our SNAP ML-IAP predictions with DFT-MD also at 5 eV (58022 K) indicating the reliability of the SNAP ML-IAP also outside the range of training data.

Finally, we illustrate the DSF at 5 eV (58022 K) for two values of the wave vector $q = 0.45 \text{ \AA}^{-1}$ and $q = 0.96 \text{ \AA}^{-1}$ in

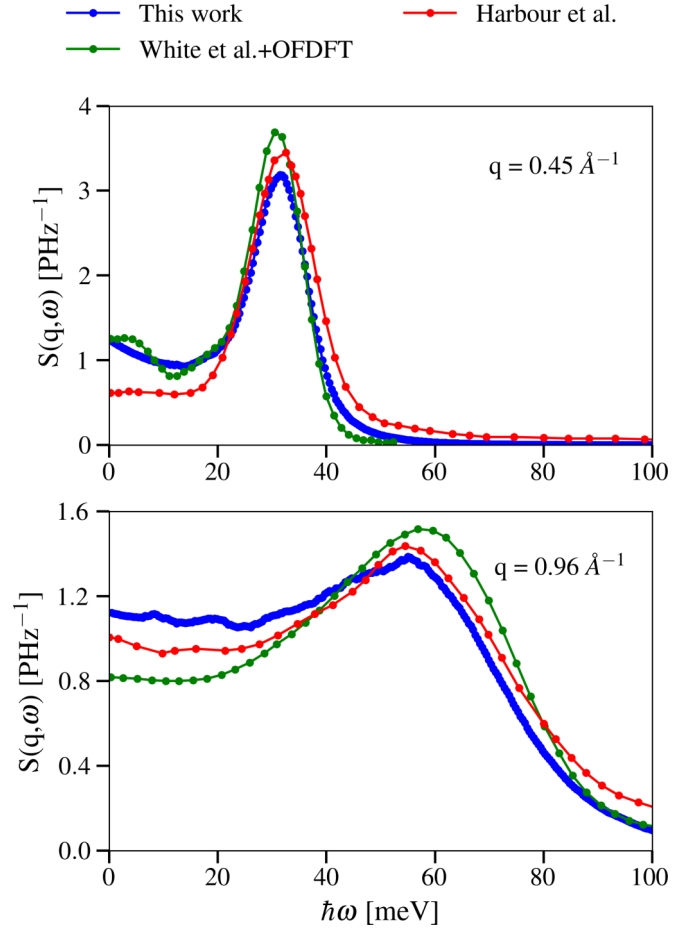


FIG. 8. Dynamic structure factor of aluminum at 2.7 g/cm^3 and 5 eV (58022 K) for wave vectors $q = 0.45 \text{ \AA}^{-1}$ (top) and $q = 0.96 \text{ \AA}^{-1}$ (bottom). Our result (blue) is compared with the OFDFT result of White *et al.* [27] (green curve) and the neutral pseudoatom (NPA) model of Harbour *et al.* [90] (red curve).

Fig. 8. Similarly, we compare our results with results from OFDFT [27] (green curve) and a neutral pseudoatom (NPA) model [90] (red curve) and find qualitative agreement. We can further assess the quality of our predictions by checking the sum rules the DSF obeys [91]. To that end, we evaluate the sum rule

$$\int_{-\infty}^{\infty} d\omega S(\mathbf{q}, \omega) = S(\mathbf{q}) = F(\mathbf{q}, 0), \quad (16)$$

which states that the SSF is recovered from the DSF by integration over the frequency domain. This is demonstrated for temperatures of 0.5 eV (5802 K) and 5 eV (58022 K) in Fig. S4 [67].

IV. CONCLUSIONS

Our study has resulted in the training of a single ML-IAP using DFT-MD data and the SNAP methodology to model the properties of aluminum in a wide range of conditions, from ambient to WDM. Previous ML-IAPs have been trained for specific temperature and pressure ranges. However, our findings demonstrate that a single ML-IAP can yield reliable and precise results across a broad temperature range.

To evaluate the transferability of our ML-IAP, we computed several material and transport properties, including the ionic part of thermal conductivity, shear viscosity, self-diffusion coefficient, sound velocity, and structure factor. Our results for the thermal conductivity and shear viscosity are consistent with previous findings from ML-IAPs [36,37,76,77], although those ML-IAPs were specifically trained for the tested temperature ranges. Regarding the self-diffusion coefficient, our predictions agree well with reference data from DFT-MD [82] and are in qualitative agreement with less accurate results from OFDFT [82] and kinetic theory [83]. Furthermore, our ML-IAP enables the determination of the sound velocity, which is otherwise difficult to compute using DFT-MD calculations due to the requirement of large simulation cells. We demonstrate these calculations for aluminum at a broad temperature range and obtain qualitative agreement with OFDFT results [27]. Lastly, we show that our ML-IAP can predict the ion-ion structure factor with the same accuracy as DFT-MD [27]. Overall, our results demonstrate the ability of our ML-IAP to yield results in line with prior research and, more importantly, its reliability and accuracy beyond the training range.

Demonstrating the transferability of an ML-IAP across a broad temperature range presents a significant advancement. Utilizing transferable ML-IAPs reduces the computational resources required to generate material properties for studying matter under elevated temperatures and enables more comprehensive and accurate simulations of materials properties. This will greatly support the interpretation of experimental measurements of laser-driven and shock-compressed samples at free-electron laser facilities worldwide. While we have shown the transferability of our ML-IAP for temperature ranges, a comprehensive ML-IAP that is useful for extended

simulations of properties in WDM requires transferability across both pressure and temperature ranges. We plan to address this challenge in our future work and further advance our methodology.

ACKNOWLEDGMENTS

This work was partially supported by the Center for Advanced Systems Understanding (CASUS), which is financed by Germany's Federal Ministry of Education and Research (BMBF) and by the Saxon state government out of the State budget approved by the Saxon State Parliament. M.L. was supported by the German Federal Ministry of Education and Research (BMBF, No. 01/S18026A-F) by funding the competence center for Big Data and AI "ScaDS.AI Dresden/Leipzig." Computations were performed on a Bull Cluster at the Center for Information Services and High Performance Computing (ZIH) at Technische Universität Dresden, on the cluster Hemera at Helmholtz-Zentrum Dresden-Rossendorf (HZDR). This article has been authored by an employee of National Technology & Engineering Solutions of Sandia, LLC under Contract No. DE-NA0003525 with the U.S. Department of Energy (DOE). The employee owns all right, title and interest in and to the article and is solely responsible for its contents. The United States Government retains and the publisher, by accepting the article for publication, acknowledges that the United States Government retains a nonexclusive, paid-up, irrevocable, world-wide license to publish or reproduce the published form of this article or allow others to do so, for United States Government purposes. The DOE will provide public access to these results of federally sponsored research in accordance with the DOE Public Access Plan [92].

-
- [1] F. Graziani, M. P. Desjarlais, R. Redmer, and S. B. Trickey, *Frontiers and Challenges in Warm Dense Matter*, Vol. 96 (Springer Science & Business, Berlin, 2014).
- [2] D. Riley, N. C. Woolsey, D. McSherry, I. Weaver, A. Djaoui, and E. Nardi, X-Ray Diffraction from a Dense Plasma, *Phys. Rev. Lett.* **84**, 1704 (2000).
- [3] T. Ma, T. Döppner, R. W. Falcone, L. Fletcher, C. Fortmann, D. O. Gericke, O. L. Landen, H. J. Lee, A. Pak, J. Vorberger, K. Wunsch, and S. H. Glenzer, X-Ray Scattering Measurements of Strong Ion-Ion Correlations in Shock-Compressed Aluminum, *Phys. Rev. Lett.* **110**, 065001 (2013).
- [4] M. Bonitz, T. Dornheim, Z. A. Moldabekov, S. Zhang, P. Hamann, H. Kählert, A. Filinov, K. Ramakrishna, and J. Vorberger, *Ab initio* simulation of warm dense matter, *Phys. Plasmas* **27**, 042710 (2020).
- [5] T. Dornheim, Z. A. Moldabekov, K. Ramakrishna, P. Tolias, A. D. Baczewski, D. Kraus, T. R. Preston, D. A. Chapman, M. P. Böhme, T. Döppner *et al.*, Electronic density response of warm dense matter, *Phys. Plasmas* **30**, 032705 (2023).
- [6] T. Guillot, Interiors of giant planets inside and outside the solar system, *Science* **286**, 72 (1999).
- [7] D. B. Sinars, M. A. Sweeney, C. S. Alexander, D. J. Ampleford, T. Ao, J. P. Apruzese, C. Aragon, D. J. Armstrong, K. N. Austin, T. J. Awe *et al.*, Review of pulsed power-driven high energy density physics research on Z at sandia, *Phys. Plasmas* **27**, 070501 (2020).
- [8] K. Voigt, M. Zhang, K. Ramakrishna, A. Amouretti, K. Appel, E. Brambrink, V. Cerantola, D. Chekrygina, T. Döppner, R. W. Falcone, K. Falk, L. B. Fletcher, D. O. Gericke, S. Göde, M. Harmand, N. J. Hartley, S. P. Hau-Riege, L. G. Huang, O. S. Humphries, M. Lokamani *et al.*, Demonstration of an x-ray raman spectroscopy setup to study warm dense carbon at the high energy density instrument of European XFEL, *Phys. Plasmas* **28**, 082701 (2021).
- [9] L. B. Fletcher, H. J. Lee, T. Döppner, E. Galtier, B. Nagler, P. Heimann, C. Fortmann, S. LePape, T. Ma, M. Millot, A. Pak, D. Turnbull, D. A. Chapman, D. O. Gericke, J. Vorberger, T. White, G. Gregori, M. Wei, B. Barbrel, R. W. Falcone *et al.*, Ultrabright x-ray laser scattering for dynamic warm dense matter physics, *Nat. Photon.* **9**, 274 (2015).
- [10] E. E. McBride, T. G. White, A. Descamps, L. B. Fletcher, K. Appel, F. P. Condamine, C. B. Curry, F. Dallari, S. Funk, E. Galtier, M. Gauthier, S. Goede, J. B. Kim, H. J. Lee, B. K. Ofori-Okai, M. Oliver, A. Rigby, C. Schoenwaelder, P. Sun, T. Tschentscher *et al.*, Setup for mev-resolution inelastic x-ray scattering measurements and x-ray diffraction at the matter in

- extreme conditions endstation at the linac coherent light source, *Rev. Sci. Instrum.* **89**, 10F104 (2018).
- [11] S. Frydrych, J. Vorberger, N. J. Hartley, A. K. Schuster, K. Ramakrishna, A. M. Saunders, T. van Driel, R. W. Falcone, L. B. Fletcher, E. Galtier *et al.*, Demonstration of x-ray thomson scattering as diagnostics for miscibility in warm dense matter, *Nat. Commun.* **11**, 2620 (2020).
- [12] C. A. Haynam, P. J. Wegner, J. M. Auerbach, M. W. Bowers, S. N. Dixit, G. V. Erbert, G. M. Heestand, M. A. Hennesian, M. R. Hermann, K. S. Jancaitis, K. R. Manes, C. D. Marshall, N. C. Mehta, J. Menapace, E. Moses, J. R. Murray, M. C. Nostrand, C. D. Orth, R. Patterson, R. A. Sacks *et al.*, National ignition facility laser performance status, *Appl. Opt.* **46**, 3276 (2007).
- [13] R. Betti and O. A. Hurricane, Inertial-confinement fusion with lasers, *Nat. Phys.* **12**, 435 (2016).
- [14] M. P. Desjarlais, J. D. Kress, and L. A. Collins, Electrical conductivity for warm, dense aluminum plasmas and liquids, *Phys. Rev. E* **66**, 025401(R) (2002).
- [15] M. P. Desjarlais, Density-functional calculations of the liquid deuterium hughoniot, reshock, and reverberation timing, *Phys. Rev. B* **68**, 064204 (2003).
- [16] S. Mazevet, M. P. Desjarlais, L. A. Collins, J. D. Kress, and N. H. Magee, Simulations of the optical properties of warm dense aluminum, *Phys. Rev. E* **71**, 016409 (2005).
- [17] N. Nettelmann, B. Holst, A. Kietzmann, M. French, R. Redmer, and D. Blaschke, Ab initio equation of state data for hydrogen, helium, and water and the internal structure of jupiter, *Astrophys. J.* **683**, 1217 (2008).
- [18] K. Ramakrishna, A. Cangi, T. Dornheim, A. Baczewski, and J. Vorberger, First-principles modeling of plasmons in aluminum under ambient and extreme conditions, *Phys. Rev. B* **103**, 125118 (2021).
- [19] T. Dornheim, A. Cangi, K. Ramakrishna, M. Böhme, S. Tanaka, and J. Vorberger, Effective Static Approximation: A Fast and Reliable Tool for Warm-Dense Matter Theory, *Phys. Rev. Lett.* **125**, 235001 (2020).
- [20] M. French, T. R. Mattsson, N. Nettelmann, and R. Redmer, Equation of state and phase diagram of water at ultrahigh pressures as in planetary interiors, *Phys. Rev. B* **79**, 054107 (2009).
- [21] M. S. Daw and M. I. Baskes, Semiempirical, Quantum Mechanical Calculation of Hydrogen Embrittlement in Metals, *Phys. Rev. Lett.* **50**, 1285 (1983).
- [22] M. S. Daw and M. I. Baskes, Embedded-atom method: Derivation and application to impurities, surfaces, and other defects in metals, *Phys. Rev. B* **29**, 6443 (1984).
- [23] S. M. Foiles, M. I. Baskes, and M. S. Daw, Embedded-atom-method functions for the fcc metals cu, ag, au, ni, pd, pt, and their alloys, *Phys. Rev. B* **33**, 7983 (1986).
- [24] G. E. Norman, S. V. Starikov, V. V. Stegailov, I. M. Saitov, and P. A. Zhilyaev, Atomistic modeling of warm dense matter in the two-temperature state, *Contrib. Plasma Phys.* **53**, 129 (2013).
- [25] Z. Chen, M. Mo, L. Souillard, V. Recoules, P. Hering, Y. Y. Tsui, S. H. Glenzer, and A. Ng, Interatomic Potential in the Nonequilibrium Warm Dense Matter Regime, *Phys. Rev. Lett.* **121**, 075002 (2018).
- [26] J. Vorberger, Z. Donko, I. M. Tkachenko, and D. O. Gericke, Dynamic Ion Structure Factor of Warm Dense Matter, *Phys. Rev. Lett.* **109**, 225001 (2012).
- [27] T. G. White, S. Richardson, B. J. B. Crowley, L. K. Pattison, J. W. O. Harris, and G. Gregori, Orbital-Free Density-Functional Theory Simulations of the Dynamic Structure Factor of Warm Dense Aluminum, *Phys. Rev. Lett.* **111**, 175002 (2013).
- [28] M. W. C. Dharma-wardana, L. J. Stanek, and M. S. Murillo, Yukawa-Friedel-tail pair potentials for warm dense matter applications, *Phys. Rev. E* **106**, 065208 (2022).
- [29] J. Behler and M. Parrinello, Generalized Neural-Network Representation of High-Dimensional Potential-Energy Surfaces, *Phys. Rev. Lett.* **98**, 146401 (2007).
- [30] A. P. Bartók, M. C. Payne, R. Kondor, and G. Csányi, Gaussian Approximation Potentials: The Accuracy of Quantum Mechanics, without the Electrons, *Phys. Rev. Lett.* **104**, 136403 (2010).
- [31] A. P. Thompson, L. P. Swiler, C. R. Trott, S. M. Foiles, and G. J. Tucker, Spectral neighbor analysis method for automated generation of quantum-accurate interatomic potentials, *J. Comput. Phys.* **285**, 316 (2015).
- [32] L. Zhang, J. Han, H. Wang, R. Car, and W. E, Deep Potential Molecular Dynamics: A Scalable Model with the Accuracy of Quantum Mechanics, *Phys. Rev. Lett.* **120**, 143001 (2018).
- [33] J. Behler, Perspective: Machine learning potentials for atomistic simulations, *J. Chem. Phys.* **145**, 170901 (2016).
- [34] D. Tisi, L. Zhang, R. Bertossa, H. Wang, R. Car, and S. Baroni, Heat transport in liquid water from first-principles and deep neural network simulations, *Phys. Rev. B* **104**, 224202 (2021).
- [35] S. Nikolov, M. A. Wood, A. Cangi, J.-B. Maillat, M.-C. Marinica, A. P. Thompson, M. P. Desjarlais, and J. Tranchida, Data-driven magneto-elastic predictions with scalable classical spin-lattice dynamics, *Npj Comput. Mater.* **7**, 153 (2021).
- [36] Y. Cheng, H. Wang, S. Wang, X. Gao, Q. Li, J. Fang, H. Song, W. Chu, G. Zhang, H. Song *et al.*, Deep-learning potential method to simulate shear viscosity of liquid aluminum at high temperature and high pressure by molecular dynamics, *AIP Adv.* **11**, 015043 (2021).
- [37] Q. Liu, J. Li, and M. Chen, Thermal transport by electrons and ions in warm dense aluminum: A combined density functional theory and deep potential study, *Matter Radiat. Extremes* **6**, 026902 (2021).
- [38] L. J. Stanek, R. C. Clay III, M. W. C. Dharma-Wardana, M. A. Wood, K. R. C. Beckwith, and M. S. Murillo, Efficacy of the radial pair potential approximation for molecular dynamics simulations of dense plasmas, *Phys. Plasmas* **28**, 032706 (2021).
- [39] M. Schörner, H. R. Rüter, M. French, and R. Redmer, Extending *ab initio* simulations for the ion-ion structure factor of warm dense aluminum to the hydrodynamic limit using neural network potentials, *Phys. Rev. B* **105**, 174310 (2022).
- [40] M. Schörner, B. B. L. Witte, A. D. Baczewski, A. Cangi, and R. Redmer, *Ab initio* study of shock-compressed copper, *Phys. Rev. B* **106**, 054304 (2022).
- [41] J. T. Willman, K. Nguyen-Cong, A. S. Williams, A. B. Belonoshko, S. G. Moore, A. P. Thompson, M. A. Wood, and I. I. Oleynik, Machine learning interatomic potential for simulations of carbon at extreme conditions, *Phys. Rev. B* **106**, L180101 (2022).
- [42] T. J. Murphy, M. R. Douglas, J. R. Fincke, R. E. Olson, J. A. Cobble, B. M. Haines, C. E. Hamilton, M. N. Lee, J. A. Oertel, N. A. G. Parra-Vasquez, R. B. Randolph, D. W. Schmidt, R. C. Shah, J. M. Smidt, and I. L. Tregillis, Progress in the development of the marble platform for studying thermonuclear burn in

- the presence of heterogeneous mix on omega and the national ignition facility, *J. Phys.: Conf. Ser.* **717**, 012072 (2016).
- [43] B. A. Buffett, Estimates of heat flow in the deep mantle based on the power requirements for the geodynamo, *Geophys. Res. Lett.* **29**, 1566 (2002).
- [44] S. Kumar, A. J. Poser, M. Schöttler, U. Kleinschmidt, W. Dietrich, J. Wicht, M. French, and R. Redmer, Ionization and transport in partially ionized multicomponent plasmas: Application to atmospheres of hot jupiters, *Phys. Rev. E* **103**, 063203 (2021).
- [45] W. Dietrich, S. Kumar, A. J. Poser, M. French, N. Nettelmann, R. Redmer, and J. Wicht, Magnetic induction processes in hot Jupiters, application to KELT-9b, *Mon. Not. R. Astron. Soc.* **517**, 3113 (2022).
- [46] S. Nikolov, J. Tranchida, K. Ramakrishna, M. Lokamani, A. Cangi, and M. A. Wood, Dissociating the phononic, magnetic and electronic contributions to thermal conductivity: A computational study in alpha-iron, *J. Mater. Sci.* **57**, 10535 (2022).
- [47] B. Adams, W. Bohnhoff, K. Dalbey, M. Ebeida, J. Eddy, M. Eldred, R. Hooper, P. Hough, K. Hu, J. Jakeman *et al.*, Dakota, A Multilevel Parallel Object-Oriented Framework for Design Optimization, Parameter Estimation, Uncertainty Quantification, and Sensitivity Analysis: Version 6.13 User's Manual, Tech. Rep., Sandia National Lab. (SNL-NM), Albuquerque, 2020.
- [48] A. McKelvey, G. E. Kemp, P. A. Sterne, A. Fernandez-Panella, R. Shepherd, M. Marinak, A. Link, G. W. Collins, H. Sio, J. King *et al.*, Thermal conductivity measurements of proton-heated warm dense aluminum, *Sci. Rep.* **7**, 7015 (2017).
- [49] B. Nagler, U. Zastrau, R. R. Fäustlin, S. M. Vinko, T. Whitcher, A. J. Nelson, R. Sobierajski, J. Krzywinski, J. Chalupsky, E. Abreu, S. Bajt, T. Bornath, T. Burian, H. Chapman, J. Cihelka, T. Döppner, S. Düsterer, T. Dzelzainis, M. Fajardo, E. Förster *et al.*, Turning solid aluminium transparent by intense soft x-ray photoionization, *Nat. Phys.* **5**, 693 (2009).
- [50] P. M. Leguay, A. Lévy, B. Chimier, F. Deneuille, D. Descamps, C. Fourment, C. Goyon, S. Hulin, S. Petit, O. Peyrusse, J. J. Santos, P. Combis, B. Holst, V. Recoules, P. Renaudin, L. Videau, and F. Dorchie, Ultrafast Short-Range Disorder of Femtosecond-Laser-Heated Warm Dense Aluminum, *Phys. Rev. Lett.* **111**, 245004 (2013).
- [51] M. Z. Mo, Z. Chen, S. Fourmaux, A. Saraf, S. Kerr, K. Otani, R. Masoud, J.-C. Kieffer, Y. Tsui, A. Ng, and R. Fedosejevs, Measurements of ionization states in warm dense aluminum with betatron radiation, *Phys. Rev. E* **95**, 053208 (2017).
- [52] P. Sperling, E. J. Gamboa, H. J. Lee, H. K. Chung, E. Galtier, Y. Omarbakiyeva, H. Reinholz, G. Röpke, U. Zastrau, J. Hastings, L. B. Fletcher, and S. H. Glenzer, Free-Electron X-Ray Laser Measurements of Collisional-Damped Plasmons in Isochorically Heated Warm Dense Matter, *Phys. Rev. Lett.* **115**, 115001 (2015).
- [53] B. B. L. Witte, L. B. Fletcher, E. Galtier, E. Gamboa, H. J. Lee, U. Zastrau, R. Redmer, S. H. Glenzer, and P. Sperling, Warm Dense Matter Demonstrating Non-Drude Conductivity from Observations of Nonlinear Plasmon Damping, *Phys. Rev. Lett.* **118**, 225001 (2017).
- [54] M. A. Wood and A. P. Thompson, Extending the accuracy of the snap interatomic potential form, *J. Chem. Phys.* **148**, 241721 (2018).
- [55] G. Kresse and J. Furthmüller, Efficient iterative schemes for ab initio total-energy calculations using a plane-wave basis set, *Phys. Rev. B* **54**, 11169 (1996).
- [56] G. Kresse and J. Furthmüller, Efficiency of *ab-initio* total energy calculations for metals and semiconductors using a plane-wave basis set, *Comput. Mater. Sci.* **6**, 15 (1996).
- [57] G. Kresse and D. Joubert, From ultrasoft pseudopotentials to the projector augmented-wave method, *Phys. Rev. B* **59**, 1758 (1999).
- [58] P. Hohenberg and W. Kohn, Inhomogeneous electron gas, *Phys. Rev.* **136**, B864 (1964).
- [59] W. Kohn and L. J. Sham, Self-consistent equations including exchange and correlation effects, *Phys. Rev.* **140**, A1133 (1965).
- [60] N. D. Mermin, Thermal properties of the inhomogeneous electron gas, *Phys. Rev.* **137**, A1441 (1965).
- [61] J. P. Perdew, K. Burke, and M. Ernzerhof, Generalized Gradient Approximation Made Simple, *Phys. Rev. Lett.* **77**, 3865 (1996).
- [62] S. Nosé, A molecular dynamics method for simulations in the canonical ensemble, *Mol. Phys.* **52**, 255 (1984).
- [63] W. G. Hoover, Canonical dynamics: Equilibrium phase-space distributions, *Phys. Rev. A* **31**, 1695 (1985).
- [64] J. F. Ziegler, J. P. Biersack, and U. Littmark, *The Stopping and Ranges of Ions in Solids*, Vol. 1 (Pergamon Press, Oxford, 1985).
- [65] FitSNAP: A python package for machine learning potentials with LAMMPS, <https://github.com/FitSNAP>.
- [66] A. Rohskopf, C. Sievers, N. Lubbers, M. Cusentino, J. Goff, J. Janssen, M. McCarthy, D. M. O. de Zapiain, S. Nikolov, K. Sargsyan *et al.*, FitSNAP: Atomistic machine learning with lammps, *J. Open Source Softw.* **8**, 5118 (2023).
- [67] See Supplemental Material at <http://link.aps.org/supplemental/10.1103/PhysRevResearch.5.033162> for details of training data sets and errors, finite-size effect, longitudinal current spectra, and dynamic structure factor sum rule.
- [68] E. L. Sikorski, M. A. Cusentino, M. J. McCarthy, J. Tranchida, M. A. Wood, and A. P. Thompson, Machine learned interatomic potential for dispersion strengthened plasma facing components, *J. Chem. Phys.* **158**, 114101 (2023).
- [69] B. M. Adams, W. J. Bohnhoff, K. R. Dalbey, J. P. Eddy, M. S. Eldred, D. M. Gay, K. Haskell, P. D. Hough, and L. P. Swiler, Dakota, a multilevel parallel object-oriented framework for design optimization, parameter estimation, uncertainty quantification, and sensitivity analysis: Version 5.0 user's manual, Sandia National Laboratories, Tech. Rep. SAND2010-2183, 2009.
- [70] The scripts and DFT-MD training datasets used to construct the SNAP ML-IAP are available at <https://rodare.hzdr.de/record/2369>.
- [71] S. Plimpton, Fast parallel algorithms for short-range molecular dynamics, *J. Comput. Phys.* **117**, 1 (1995).
- [72] M. S. Green, Markoff random processes and the statistical mechanics of time-dependent phenomena. ii. irreversible processes in fluids, *J. Chem. Phys.* **22**, 398 (1954).
- [73] R. Kubo, Statistical-mechanical theory of irreversible processes. I. general theory and simple applications to magnetic and conduction problems, *J. Phys. Soc. Jpn.* **12**, 570 (1957).
- [74] M. T. Humbert, Y. Zhang, and E. J. Maginn, PyLAT: Python lammps analysis tools, *J. Chem. Inf. Model.* **59**, 1301 (2019).

- [75] B. Cheng and D. Frenkel, Computing the Heat Conductivity of Fluids from Density Fluctuations, *Phys. Rev. Lett.* **125**, 130602 (2020).
- [76] Y. Zhou, B. Anglin, and A. Strachan, Phonon thermal conductivity in nanolaminated composite metals via molecular dynamics, *J. Chem. Phys.* **127**, 184702 (2007).
- [77] N. Stojanovic, D. H. S. Maithripala, J. M. Berg, and M. Holtz, Thermal conductivity in metallic nanostructures at high temperature: Electrons, phonons, and the wiedemann-franz law, *Phys. Rev. B* **82**, 075418 (2010).
- [78] S. X. Hu, B. Militzer, L. A. Collins, K. P. Driver, J. D. Kress *et al.*, First-principles prediction of the softening of the silicon shock hugoniot curve, *Phys. Rev. B* **94**, 094109 (2016).
- [79] K. P. Driver, F. Soubiran, and B. Militzer, Path integral monte carlo simulations of warm dense aluminum, *Phys. Rev. E* **97**, 063207 (2018).
- [80] S. Zhang, B. Militzer, L. X. Benedict, F. Soubiran, P. A. Sterne, and K. P. Driver, Path integral monte carlo simulations of dense carbon-hydrogen plasmas, *J. Chem. Phys.* **148**, 102318 (2018).
- [81] B. Scheiner and S. D. Baalrud, Testing thermal conductivity models with equilibrium molecular dynamics simulations of the one-component plasma, *Phys. Rev. E* **100**, 043206 (2019).
- [82] T. Sjostrom and J. Daligault, Ionic and electronic transport properties in dense plasmas by orbital-free density functional theory, *Phys. Rev. E* **92**, 063304 (2015).
- [83] J. Daligault, S. D. Baalrud, C. E. Starrett, D. Saumon, and T. Sjostrom, Ionic Transport Coefficients of Dense Plasmas without Molecular Dynamics, *Phys. Rev. Lett.* **116**, 075002 (2016).
- [84] J.-P. Hansen and I. R. McDonald, *Theory of Simple Liquids: With Applications to Soft Matter* (Academic Press, New York, 2013).
- [85] M. M. G. Alemany, L. J. Gallego, and D. J. González, Kohnsham *ab initio* molecular dynamics study of liquid Al near melting, *Phys. Rev. B* **70**, 134206 (2004).
- [86] J.-P. Hansen, I. R. McDonald, and E. L. Pollock, Statistical mechanics of dense ionized matter. III. dynamical properties of the classical one-component plasma, *Phys. Rev. A* **11**, 1025 (1975).
- [87] S. H. Glenzer and R. Redmer, X-ray thomson scattering in high energy density plasmas, *Rev. Mod. Phys.* **81**, 1625 (2009).
- [88] H. R. Rüter and R. Redmer, *Ab Initio* Simulations for the Ion-Ion Structure Factor of Warm Dense Aluminum, *Phys. Rev. Lett.* **112**, 145007 (2014).
- [89] E. Fransson, M. Slabanja, P. Erhart, and G. Wahnström, DYNASOR—a tool for extracting dynamical structure factors and current correlation functions from molecular dynamics simulations, *Adv. Theory Simul.* **4**, 2000240 (2021).
- [90] L. Harbour, G. D. Förster, M. W. C. Dharma-Wardana, and L. J. Lewis, Ion-ion dynamic structure factor, acoustic modes, and equation of state of two-temperature warm dense aluminum, *Phys. Rev. E* **97**, 043210 (2018).
- [91] J. F. Wax and T. Bryk, An effective fitting scheme for the dynamic structure of pure liquids, *J. Phys.: Condens. Matter* **25**, 325104 (2013).
- [92] <https://www.energy.gov/downloads/doe-public-access-plan>.